Temperature and heating rate of ion crystals in Penning traps

Marie J. Jensen,* Taro Hasegawa,† and John J. Bollinger
National Institute of Standards and Technology, Boulder, Colorado 80305, USA
(Received 1 April 2004; published 3 September 2004)

We have determined the temperature and heating rate of laser-cooled ions in a Penning trap using Doppler laser spectroscopy. Between 10^4 and 10^6 $^9Be^+$ ions are trapped in a Penning trap and Doppler laser cooled to temperatures of a few millikelvin, where they form ion crystals. This system is an example of a strongly coupled one-component plasma. The ion temperature was measured as a function of time after turning off the laser-cooling. In the solid phase, we measured a heating rate of ~65 mK/s. Information about possible heating mechanisms was obtained directly from temperature measurements, and also from measurements of the rate of radial expansion of the ion plasma. We determined that the observed heating is due to collisions with the $\sim 4\times 10^{-9}$ Pa residual gas of our vacuum system.

DOI: 10.1103/PhysRevA.70.033401 PACS number(s): 32.80.Pj, 03.67.Mn, 52.27.Gr, 52.27.Jt

I. INTRODUCTION

Plasmas of ions trapped in either Paul or Penning traps are routinely laser cooled to temperatures sufficiently low for the plasma to enter the liquid or solid phases [1–4]. These cold ion plasmas offer unique possibilities for studies of both atomic physics and strongly coupled plasma physics with related applications as diverse as cold antimatter, low-temperature chemistry, high-precision atomic and molecular spectroscopy, frequency standards, and quantum information processing [5]. Because the confinement in a Penning trap is provided by static electric and magnetic fields, the Penning trap is particularly well suited for trapping and cooling large numbers of ions. We trap up to $\sim 10^6$ $^9Be^+$ ions in a Penning trap and laser cool these ions to below 10 mK, where the ion plasma undergoes a phase transition to the solid phase and forms a crystal with an interparticle spacing on the order of 10 μm [2,3].

A laser-cooled ion plasma in a Penning trap provides a clean, rigorous realization of a one-component plasma (OCP). An OCP is a system of a single species of classical point charges (ions) embedded in a uniform neutralizing background charge [6–8]. The thermodynamic state of an OCP is determined by the coupling parameter Γ which is defined as

$$\Gamma = \frac{1}{4\pi\epsilon_0}\frac{q^2}{a_{\mathrm{WS}}k_B T}, \tag{1}$$

where ϵ_0 is the vacuum permittivity, q is the ion charge, k_B is Boltzmann's constant, T is the temperature, and a_{WS} is the Wigner-Seitz radius given by the expression for the plasma density $n_0 = 3/(4\pi a_{\mathrm{WS}}^3)$. Γ is a dimensionless measure of the ratio of the potential energy between nearest-neighbor ions to the ion thermal energy. Strongly coupled OCPs ($\Gamma > 1$) are believed to exist in dense astrophysical objects such as in the crust of a neutron star, where iron nuclei are embedded in a degenerate electron gas. They can also exist in less dense objects, however, only if the temperature is correspondingly low. Cold trapped ions form a convenient low-density and low-temperature strongly coupled laboratory OCP. With ions trapped in a Penning trap, the uniform neutralizing background charge is provided by the trapping potential [8,9]. OCPs have been subject to extensive theoretical and computational studies. For instance, the coupling parameter where the plasma undergoes the liquid-solid phase transition has been determined to high accuracy. In recent years, the calculations have converged to $\Gamma \simeq 172-174$ [7,10]. There is no corresponding experimental determination of this value. In fact, the actual liquid-solid phase transition has never been directly observed in an OCP.

Due to the crossed electric and magnetic fields in a Penning trap, the trapped ion plasma undergoes a rotation about the magnetic-field axis. In thermal equilibrium, this rotation is rigid [8]. At the low temperatures characterizing the present work, the plasma density n_0 is constant within the plasma boundary and can be expressed as

$$n_0 = 2\epsilon_0 m\omega_r(\Omega_c - \omega_r)/q^2, \tag{2}$$

where m is the ion mass, ω_r is the rotation frequency about the magnetic-field axis, and Ω_c is the cyclotron frequency. Accordingly, the density is determined by the rotation frequency. At the plasma boundary, the density decreases from this constant value to zero over a distance comparable to the Debye length $\lambda_D = \sqrt{\epsilon_0 k_B T/n_0 q^2}$, which for the present system is shorter than the interparticle spacing. Due to the quadratic trapping potential, the plasma is shaped like a spheroid with an aspect ratio $\alpha \equiv z_0/r_0$. Here $2z_0$ is the axial extent, i.e., the extent along the magnetic-field axis, of the cloud at $r=0$, and the equation $z(r) = \pm\alpha\sqrt{r_0^2 - r^2}$ describes the boundary of the cloud. The aspect ratio is directly related to the rotation frequency ω_r [8]. The stability region of the trap, in terms of rotation frequency, is $\omega_m < \omega_r < \Omega_c - \omega_m$, where ω_m is the single-ion magnetron frequency.

Here, we present measurements of the trapped-ion temperature for motion parallel to the magnetic field as well as the rate at which this temperature increases when no laser

*Electronic address: mjensen@boulder.nist.gov
†Present address: University of Hyogo, Hyogo 678-1297, Japan

cooling is applied, i.e., the heating rate (see Secs. II A and III A). We focus on the solid-phase behavior. This work is motivated mainly by the prospects of creating many-particle entangled states. Entanglement can lead to improved spectroscopic precision. For an ensemble of independently prepared ions, the uncertainty on a given transition frequency scales as $1/\sqrt{N}$, where N is the number of ions, whereas for certain entangled states, known as spin-squeezed states, the scaling can be as strong as $1/N$ [11–13]. Hence, by entangling the ions, the spectroscopic precision can potentially be improved by orders of magnitude. Also, entanglement is one of the key components required for quantum information processing. The creation of many-particle entangled states therefore has interesting implications for experiments on quantum simulation and quantum computation.

A necessary condition in the proposed schemes for creating entangled states is that the ions are in the Lamb-Dicke limit while their internal and motional states are manipulated to create the entanglement [14–16]. The Lamb-Dicke limit is the limit in which the amplitude of the ion motion in the propagation direction of the state-manipulating radiation is much less than $\lambda/2\pi$, where λ is the radiation wavelength. This constraint is basically equivalent to imposing an upper limit to the ion temperature. It is not possible to carry out the desired state manipulations while directly laser cooling the ions. Therefore, entanglement can be obtained only if the system is cold initially and has a heating rate low enough that the ions will remain in the Lamb-Dicke limit throughout the process. Here, we do not consider the option of sympathetically cooling the ions [17].

The only previously published measurements of ion heating in a Penning trap were made almost 2 decades ago on small plasmas of less than a few thousand ions [18]. The heating was not measured at short times. Instead, over a period of $\sim$10 s the ion temperature was observed to increase to $\sim$20 K. This large temperature increase was thought to be due to a radial expansion of the plasma, which occurred when the cooling laser beam directed perpendicular to the magnetic field was turned off. This beam applied a torque that maintained a constant rotation frequency ω_r (and therefore a constant plasma density and radius) by offsetting ambient torques that otherwise would decrease ω_r and increase r_0. With the perpendicular cooling beam blocked, the plasma expanded, which resulted in a conversion of Coulomb potential energy to thermal energy. This expansion has been significantly reduced in subsequent Penning traps through better trap construction and by aligning the magnetic field with the trap electrode symmetry axis. Furthermore, we currently use a rotating electric field [19] to precisely control the plasma rotation frequency and eliminate the plasma expansion. However, the rotating electric field (frequently called a "rotating wall") does work and therefore provides a source of energy or heat for the plasma [8].

In addition to measuring the ion temperature and overall heating rate, we have investigated several potential sources of the observed heating. In particular, we have considered heating due to residual-gas collisions, due to the work or energy input of the rotating electric field used to keep the plasma rotation frequency constant, and also due to noise from the trap electrodes. Temperatures measured at different residual gas pressures show the effect of residual-gas collisions and are described in Secs. II A and III B 1. Ambient static field errors due to asymmetries in the construction of the trap produce a torque on a rotating Penning trap plasma, which leads to a reduction or "spin down" of the plasma rotation. Residual gas collisions also produce a drag on the rotating plasma and contribute to the spin down. In this work, we apply a rotating electric field (a rotating wall) that opposes these spin-down torques and holds the plasma rotation frequency constant. We estimate the torque and, hence, the energy input due to the rotating wall by measuring the spin-down rate and subsequent radial expansion of the ion plasma when the rotating wall is turned off. The spin-down measurements are described in Secs. II B and III B 2. We also discuss the possibility that noise from the trap electrodes due to, e.g., fluctuating patch fields could produce heating of the ions. This is thought to be a possible heating mechanism in experiments using a few ions in miniature radio-frequency traps [20]. As discussed in Sec. III B, our measurements indicate that the heating of the ions immediately after turning off the cooling laser beams is dominated by collisional energy exchange with the room-temperature residual-gas particles.

II. EXPERIMENT

A cylindrical Penning trap is used to confine between 10^4 and 10^6 $^9Be^+$ ions at densities on the order of 2×10^8 cm^{-3} [21,22]. Figure 1 is a schematic diagram of the setup. The data presented here were, unless otherwise mentioned, recorded at a pressure of $\sim4\times10^{-9}$ Pa (see discussion of pressure measurements in the Appendix). A magnetic field of 4.5 T is provided by a superconducting solenoid. The cyclotron frequency is $\Omega_c=2\pi\times7.6$ MHz, and with a typical trapping voltage $V_{\text{trap}}=500$ V, the axial and magnetron frequencies are respectively $\omega_z=2\pi\times565$ kHz and $\omega_m=2\pi\times21$ kHz. The symmetry axis of the trap electrodes is aligned with the magnetic-field axis to within $<0.005°$. This is done by minimizing the strength of zero-frequency modes excited by a misalignment of the trap electrode and magnetic field axes [23].

Doppler laser cooling to $T<5$ mK leads to a coupling parameter $\Gamma>300$, and the plasma is therefore in the solid state. Cooling laser beams are sent through the center of the trap both parallel and perpendicular to the magnetic-field axis. These two cooling beams are derived from the same 313 nm beam which is produced by frequency doubling a 626 nm beam from a dye laser. The parallel cooling beam has a $\sim$1 mm waist [24], which is greater than the plasma radius r_0. The waist of the perpendicular cooling beam is significantly narrower (~50 μm), and this beam, if offset from the center, can be used to apply a torque on the plasma and change its rotation frequency. For the temperature measurements discussed in this paper, the cooling laser powers were around 100 and 10 μW for the parallel and perpendicular beams, respectively. In the spin-down measurements, recorded with the parallel cooling beam only, the power in this beam was lowered to around 25 μW. In all cases, the maximum intensity of the beams is below saturation of the cooling transition.

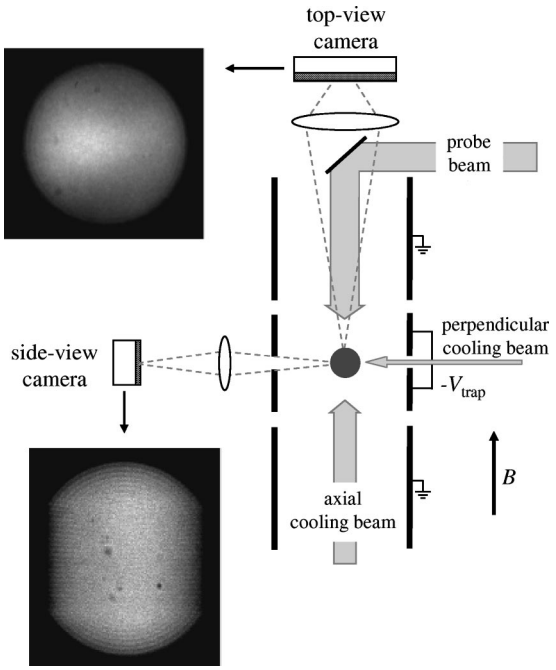

FIG. 1. Schematic diagram of setup. Figure is not to scale. The trap diameter is 4 cm. The electrodes used to apply the rotating wall field are not shown. The vertical edges of the plasma visible in the side-view image are due to the presence of nonfluorescing impurity ions heavier than Be. The direction of the side-view light collection and the direction of the perpendicular cooling beam form a 60° angle in a plane perpendicular to the magnetic field axis. Top- and side-view images of a plasma with 26 000 ions are shown. Individual crystalline planes are visible in the side-view image. The diameter of the fluorescing part of the plasma, i.e., the Be^+ ions, is 500 μm

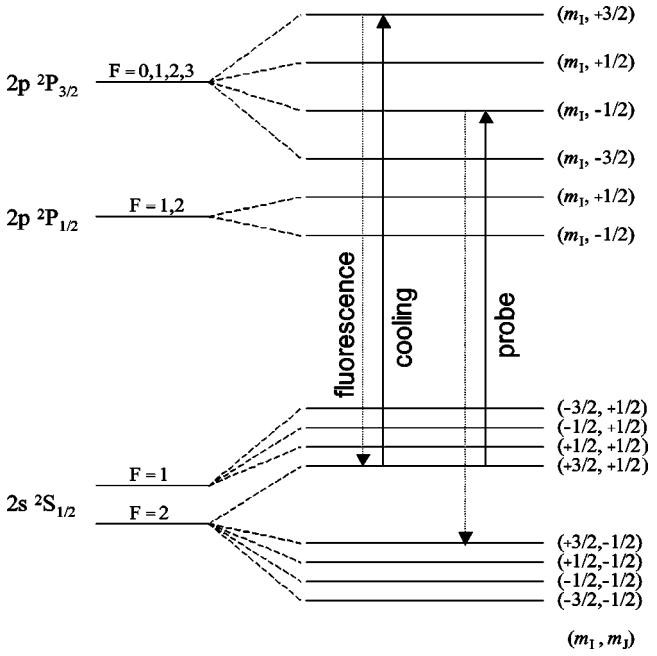

FIG. 2. Energy-level diagram for $^9Be^+$ in a high magnetic field (not to scale). Due to the very small hyperfine splittings in the P states, each line here represents all hyperfine levels, i.e., all possible values of m_I. The cooling and probe transitions are indicated. The wavelength of both laser beams is 313 nm. All diagnostics are based on the fluorescence from the cooling transition.

Doppler laser-cooling is carried out on the $^2S_{1/2}\left(m_I=+\frac{3}{2},m_J=+\frac{1}{2}\right)\leftarrow{}^2P_{3/2}\left(m_I=+\frac{3}{2},m_J=+\frac{3}{2}\right)$ transition (see Fig. 2) by use of linearly polarized light with the polarization axis perpendicular to the magnetic field axis. The cooling radiation optically pumps 96% of the ions into the $^2S_{1/2}\left(+\frac{3}{2},+\frac{1}{2}\right)$ state, i.e., the lower level of the cooling transition [25]. The parallel and perpendicular cooling beams cool the motion parallel and perpendicular, respectively, to the magnetic-field axis. Due to the Coulomb interaction between the ions, there is some coupling and, hence, sympathetic cooling between these two directions. However, to achieve the lowest ion temperatures in both the parallel and perpendicular motions, we directly laser cool in both these directions. The lowest achievable temperature using Doppler laser cooling (the Doppler-cooling limit) is $T_D=\hbar\gamma/2k_B$, where γ is the decay rate of the upper state. For the present transition the decay rate has been determined theoretically to be $\gamma=2\pi\times 18.0$ MHz [26], which leads to a Doppler-cooling limit of 0.43 mK. This limit is reached when the laser is detuned below the resonance by the amount $\gamma/2$. The data presented here were recorded at a larger detuning, but the dependence of the cooling limit on the detuning is relatively weak at detunings larger than $\gamma/2$, and the actual cooling limit should still be below 1 mK [27].

All the diagnostics are based on the ion fluorescence from the cooling-laser beams. Real-space images of the plasma are obtained both from the side, by use of a position-sensitive photomultiplier tube, and from the top, by use of a charge coupled device camera equipped with an image intensifier. The solid angles of the light collection of the side- and top-view objectives are $f/5$ and $f/2$, respectively. Phase-locked control of the rotation frequency ω_r is obtained by applying a rotating wall potential to a segmented ring electrode around the center of the trap [19]. Control of the rotation frequency implies control of the plasma density and aspect ratio. The parallel cooling beam is aligned with the magnetic field axis (the plasma rotation axis) to within $\sim 0.001°$. This alignment is done by using the perpendicular cooling beam to increase the plasma rotation frequency to near the cyclotron frequency. A slight misalignment of the parallel cooling beam produces a component of the parallel beam k vector in a direction perpendicular to the magnetic-field axis. For $\omega_r \sim \Omega_c$, the ion rotation velocity is sufficiently large that such a component, through the Doppler effect, will produce an asymmetric fluorescence visible in the top-view image.

In addition to $^9Be^+$ ions, heavier ions are slowly created by collisions between $^9Be^+$ and the residual gas. The period for 50% of the $^9Be^+$ ions to be converted into heavier ions is much greater than 100 h. Cyclotron-resonance spectroscopy has shown that these ions are predominantly of masses 10 (presumably BeH^+), 26, and 34 a.m.u.. The plasma rotation causes ions of different masses to centrifugally separate and the heavy-mass impurity ions occupy a region at larger radii. This is evident in the side-view image in Fig. 1. Since the shape of the overall plasma including impurity ions is a spheroid, we conclude that the impurity ions have the same rotation frequency as the $^9Be^+$ ions. Furthermore, the fact

that the rotating wall potential can gain phase-locked control of the plasma rotation frequency indicates that most of the impurity ions have crystallized. From this, we infer that the heavy-mass impurity ions, through sympathetic cooling, are cooled to temperatures similar to the $^9Be^+$ ions. The work presented here has typically been carried out on plasmas with 5%–20% heavy-mass impurity ions, although the data recorded at elevated residual gas pressures were obtained with plasmas having ~50% heavy-mass impurity ions.

A. Temperature measurements

The axial temperature of the $^9Be^+$ ions was probed by Doppler laser spectroscopy on the single-photon transition $^2S_{1/2}\left(m_I=+\frac{3}{2},m_J=+\frac{1}{2}\right)\leftarrow{}^2P_{3/2}\left(m_I=+\frac{3}{2},m_J=-\frac{1}{2}\right)$ [25] (see Fig. 2). The linearly polarized probe beam (waist ~1.2 mm) was sent into the trap along the magnetic field axis, and consequently the measurement provides a determination of the axial temperature. Since the probe transition is 160 GHz below the cooling transition, a second frequency-doubled dye-laser system is needed to produce the probe beam. The upper state $^2P_{3/2}\left(+\frac{3}{2},-\frac{1}{2}\right)$ decays with probability 1/3 to the $^2S_{1/2}\left(+\frac{3}{2},+\frac{1}{2}\right)$ state and with probability 2/3 to the $^2S_{1/2}\left(+\frac{3}{2},-\frac{1}{2}\right)$ state. Hence, the resonance can be observed as a decrease in fluorescence from the cooling laser due to a depopulation of the cooling laser cycle.

The data-taking procedure is as follows. At $t=0$, the cooling laser beams are turned off. After a desired amount of time, t_{delay}, the ions are exposed to a 50–500 nW probe laser pulse of duration 10 ms. Immediately thereafter the cooling laser beams are turned back on. The count rate in the side-view camera is measured before turning off (y_{before}) and after turning back on (y_{after}) the cooling beams, and the measured signal, defined as $y_{\mathrm{after}}/y_{\mathrm{before}}$, is the probability of an ion staying in the $^2S_{1/2}\left(+\frac{3}{2},+\frac{1}{2}\right)$ state. After such a measurement, the ions are exposed to the cooling beams for about 25 s. Because the cooling beams optically pump the population trapped in the $^2S_{1/2}\left(+\frac{3}{2},-\frac{1}{2}\right)$ state back to the cooling transition [25], this reinitializes the system. This cycle is repeated for different probe frequencies until the line profile has been recorded. Mechanical shutters are used for turning on and off the laser beams.

At time $t=t_{\mathrm{delay}}$ (the start of the probe laser pulse), the population is, due to the optical pumping by the cooling laser, in the $^2S_{1/2}\left(+\frac{3}{2},+\frac{1}{2}\right)$ state. For $t_{\mathrm{delay}}<t<t_{\mathrm{delay}}+10$ ms, the probe laser beam is on and the cooling laser off, which changes the probability ρ of finding an ion in the $^2S_{1/2}\left(+\frac{3}{2},+\frac{1}{2}\right)$ state by

$$\frac{d\rho}{dt}=-\tilde{a}V(\nu)\rho. \tag{3}$$

Here, $\tilde{a}$ is a proportionality constant and $V(\nu)$ is the Voigt function,

$$V(\nu)=\int_{-\infty}^{\infty}du\frac{e^{-u^2}}{\left[\dfrac{\nu-\nu_0}{\Delta\nu_D}-u\right]^2+\dfrac{1}{4}\left[\dfrac{\gamma}{2\pi\Delta\nu_D}\right]^2}, \tag{4}$$

which is a convolution of a Lorentzian and a Gaussian. ν is the laser frequency, ν_0 is the center frequency of the probe transition, γ is the Lorentzian width, and $\Delta\nu_D$ is the Gaussian width. The Lorentzian contribution is due to the natural linewidth of the transition, while the Gaussian contribution is due to Doppler broadening. From Eq. (3), the probability of an ion remaining in the $^2S_{1/2}\left(+\frac{3}{2},+\frac{1}{2}\right)$ state by the end of the 10 ms probe laser pulse is given by $\rho=e^{-\tilde{a}V(\nu)\times 10\ \mathrm{ms}}$. We therefore use the line profile

$$f(\nu)=e^{-aV(\nu)}, \tag{5}$$

to fit the measured Doppler broadened line profiles. The parameter $a=\tilde{a}\times 10$ ms determines the amplitude of the line profile.

In the fit of Eq. (5) to the measured line profile, the Lorentzian width is fixed at the theoretical value $\Delta\nu_L=\gamma/2\pi=18.0$ MHz [26], and the Gaussian width $\Delta\nu_D$ is extracted from the fit. The remaining free parameters are the amplitude a and, since frequencies are measured only on a relative scale, the center frequency ν_0. Also, the base line, which in principle should equal 1, is allowed to vary in the fit. The temperature is calculated from the expression for the Doppler width

$$\Delta\nu_D=\frac{\nu_0}{c}\sqrt{\frac{2k_BT}{m}}. \tag{6}$$

Note that for small amplitudes

$$f(\nu)\simeq 1-aV(\nu) \tag{7}$$

is just a Voigt profile. Equation (5) contains corrections due to the saturation and broadening that occurs at large amplitudes. Since only a few photon scattering events per ion during the 10 ms period are sufficient to transfer an ion from the $^2S_{1/2}\left(+\frac{3}{2},+\frac{1}{2}\right)$ to the $^2S_{1/2}\left(+\frac{3}{2},-\frac{1}{2}\right)$ state, we achieve large-amplitude signals and saturation at very low probe laser powers. In the derivation of Eq. (5), it is assumed that all ions are subject to the same probe laser power. This assumption is valid for the liquid phase, where there is good mixing of the ions within the plasma boundary. However, even for the solid phase it will be approximately valid because the waist of the probe laser beam is greater than the plasma radius r_0. A set of line profiles for very different probe laser powers were recorded for a spherical plasma of 26 000 ions, and the Gaussian widths extracted from the saturation corrected fits were independent of probe-laser power. We therefore conclude that the error in analysis caused by the assumption of uniform probe laser power is negligible.

The temperature measurements presented here were carried out at a fixed rotation frequency, $\omega_r=2\pi\times 64$ kHz corresponding to a spherical plasma, set by the rotating wall. In order to ensure a constant rotation frequency, the rotating wall does work by balancing any external torques on the plasma. In the following section, the method for measuring the magnitude of external torques is discussed.

B. Spin-down measurements

We determine the magnitude of the external torque, due to ambient static field errors and residual gas drag, by measuring the spin down of the plasma after turning off the rotating

wall and calculating the resulting change in the canonical angular momentum of the plasma. The total canonical angular momentum per ion about the magnetic-field axis of a spheroidal plasma in a Penning trap can be expressed as

$$L = \frac{3}{20}\frac{Nm}{\pi n_0 z_0}(\Omega_c - 2\omega_r), \tag{8}$$

where N is the number of ions in the plasma [8]. We wish to determine the average torque per ion

$$\tau(\omega_r) = \frac{dL}{dt}(\omega_r) \tag{9}$$

due to a change in ω_r. We here consider the torque on the entire plasma including heavy-mass impurity ions located at larger radii. Equation (8) assumes that the plasma is a pure one-species plasma. However, due to the mass dependence of Ω_c and the fact that $\Omega_c \gg \omega_r$, the mass dependence of the angular momentum and therefore also of the torque is weak. Hence, Eqs. (8) and (9) are a good approximation for the present plasmas. Using Eqs. (2) and (8), the torque per ion can be written as

$$\tau(\omega_r) = -\frac{3}{40}\frac{Ne^2}{\pi\epsilon_0 z_0}\frac{1}{\omega_r(\Omega_c - \omega_r)}\left[\frac{(\Omega_c - 2\omega_r)^2}{\omega_r(\Omega_c - \omega_r)} + \frac{(\Omega_c - 2\omega_r)}{z_0}\frac{dz_0}{d\omega_r} + 2\right]\frac{d\omega_r}{dt}. \tag{10}$$

z_0, $dz_0/d\omega_r$, and $d\omega_r/dt$ should all be taken as functions of ω_r. Accordingly, a determination of $\tau(\omega_r)$ requires knowing N, ω_r, $z_0(\omega_r)$, $(dz_0/d\omega_r)(\omega_r)$, and $(d\omega_r/dt)(\omega_r)$. With the present sign convention, a decrease in rotation frequency corresponds to a negative value of $(d\omega_r/dt)(\omega_r)$ and a positive value of $\tau(\omega_r)$.

The derivative $(d\omega_r/dt)$ represents the spin-down rate, and is measured by recording a sequence of side-view images as a function of time after turning off the rotating wall. Typically, an image with an accumulation time of 30 s is recorded every 60 s. Due to the direct relation between the rotation frequency ω_r and the plasma aspect ratio [8], a measurement of the plasma height $2z_0$ yields the value of ω_r. We choose to use the plasma height as opposed to the plasma width because the presence of nonfluorescing heavy-mass impurity ions at the largest radii complicates an accurate determination of the plasma width. The sharpness of the plasma boundary makes it possible to measure the plasma height $2z_0$ simply as the difference between the plasma top and bottom in a side-view image. In detail, a vertical slice from the center of the plasma in the 256×256 pixel side-view image is selected and projected onto the z axis (the magnetic-field axis). An example of this procedure is shown in Fig. 3. After background subtraction, the edges are found as the points where the count rate equals a certain fraction (typically 0.3) of the averaged count rate at the center plateau. Subpixel resolution is obtained by linearly interpolating between count rates in the two pixels on either side of the limit defining an edge. The actual relation between the plasma height and rotation frequency, $2z_0(\omega_r)$ [or $\omega_r(2z_0)$], is obtained from a series of calibration images recorded at known rotation frequencies.

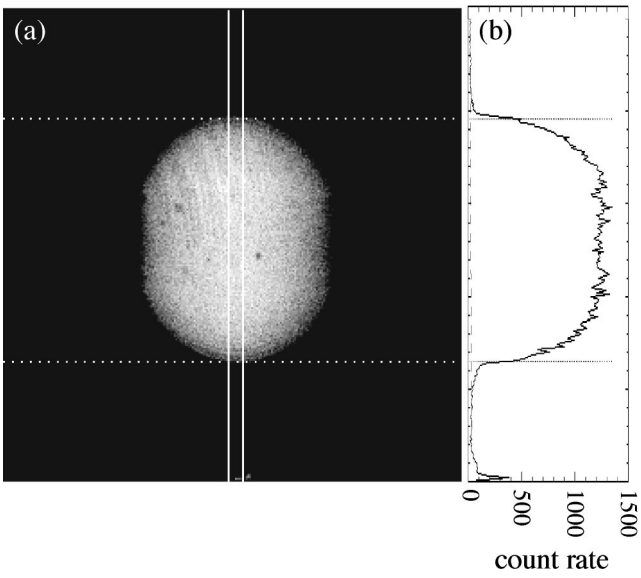

FIG. 3. (a) Side-view image with solid lines indicating the vertical slice used to determine the top and bottom of the plasma. The image size is 256×256 pixels where one pixel corresponds to a distance of 4 μm. The dotted lines indicate the top and bottom of the plasma determined by the procedure described in the text. (b) Projection of counts in the slice onto the z axis. The dotted lines indicate the position of edges while the dashed near-vertical line to the far left shows the background level which is found by linear interpolation between the background plateaus above and below the plasma.

Returning to the determination of $\tau(\omega_r)$, the calibration images yield $z_0(\omega_r)$ and $(dz_0/d\omega_r)(\omega_r)$, and the actual spin-down images in turn yield ω_r and $(d\omega_r/dt)(\omega_r)$. Calibration and spin-down images are recorded on the same plasmas with roughly equal count rate levels and analyzed following the exact same procedure in order to minimize the sensitivity to small errors in the background subtraction. The number of ions, N, is calculated from a side-view image of a spherical plasma ($\omega_r = 2\pi\times64$ kHz). The plasma height is measured and the number of ions is calculated using the relation $N = \frac{4}{3}\pi n_0 z_0^3$ together with Eq. (2).

Since the spin-down measurements are based on fluorescence images, the axial cooling beam is on during the measurements (the perpendicular cooling beam is turned off). Consequently, in addition to the external torques τ_{ext}, due to ambient static field errors and residual gas drag acting on the plasma, there can be a torque τ_{laser} caused by a small misalignment of the axial cooling beam. Even though this beam is aligned with the magnetic-field axis to within $\sim0.001°$, τ_{laser} turned out to be significant compared to τ_{ext}. To separate the contributions τ_{ext} and τ_{laser}, we alternate between recording a sequence of spin-down images with the axial cooling beam on continuously, leading to a total torque $\tau_{\text{cont}} = \tau_{\text{ext}} + \tau_{\text{laser}}$, and a sequence with the axial cooling beam chopped at 200 Hz (50% duty cycle), leading to a torque $\tau_{\text{chop}} = \tau_{\text{ext}} + \frac{1}{2}\tau_{\text{laser}}$. The external torque and the laser torque can then be determined from the equations

$$\tau_{\text{ext}} = 2\tau_{\text{chop}} - \tau_{\text{cont}},$$

$$\tau_{\text{laser}} = 2(\tau_{\text{cont}} - \tau_{\text{chop}}). \tag{11}$$

Finally, if the plasma can always be described by a (rigid-rotor) thermal equilibrium state and any changes in this state due to the coupling with the rotating wall occur adiabatically, then the energy increase per ion due to the work done by the rotating wall is given by [8]:

$$\left.\frac{dE}{dt}\right|_{\text{wall}} = \tau_{\text{ext}}\omega_r. \tag{12}$$

Here E denotes the total plasma energy (sum of the potential and kinetic energies) per ion. Specifically E is the total energy per ion as calculated in the lab frame (as opposed to the rotating frame—see the Appendix and Ref. [8]). We use Eq. (12) to estimate the possible temperature increase due to the work done by the rotating wall. We believe the assumptions of thermal equilibrium and adiabatic change that go into Eq. (12) are reasonable for the measurements discussed in this paper. These assumptions mean, for example, that the rotating wall does not excite large amplitude plasma modes, so that the plasma remains close to a thermal equilibrium state during its evolution.

III. RESULTS AND DISCUSSION

A. Determination of heating rate

Figure 4 shows two examples of measured line profiles and corresponding Voigt profile fits. The profile recorded at $t_{\text{delay}}=0$ [see Fig. 4(a)] is, ignoring the 10 ms duration of the probe pulse, a measure of the temperature when the ions are laser-cooled continuously. From the fit we determined a temperature of $T=1.6\pm0.6$ mK, which is close to the Doppler-cooling limit. The accuracy of this temperature measurement is limited by the stability of the probe laser frequency and by the fact that, at the lowest temperatures, the natural linewidth of the transition is significantly larger than the Doppler width. At higher temperatures the Doppler width dominates [see Fig. 4(b)], resulting in much smaller relative uncertainties on the extracted temperatures.

Heating-rate curves were obtained by measuring the temperature as a function of delay time t_{delay} after turning off the cooling laser. Figure 5(a) shows heating-rate curves for plasmas of 28 500 and 440 000 ions. Initially, the heating rate is slow. However, at $t_{\text{delay}}\simeq 100$ ms, in the case of 440 000 ions, the temperature increases to $T\sim 2$ K within about 100 ms. A similar behavior is observed for the plasma consisting of 28 500 ions. In both cases, the onset of this rapid heating coincides with reaching $T\sim 10$ mK. With our density of 2×10^8 cm^{-3}, $T=10$ mK corresponds to a coupling $\Gamma\sim 170$. This is where the solid-liquid phase transition of a strongly coupled plasma is predicted to take place. We therefore believe the rapid increase in the heating at $T\sim 10$ mK is due to the solid-liquid phase transition. At present we do not understand the cause of this rapid heating, and therefore in the following we focus on the short-term heating rate, i.e., the heating rate characteristic of the solid phase.

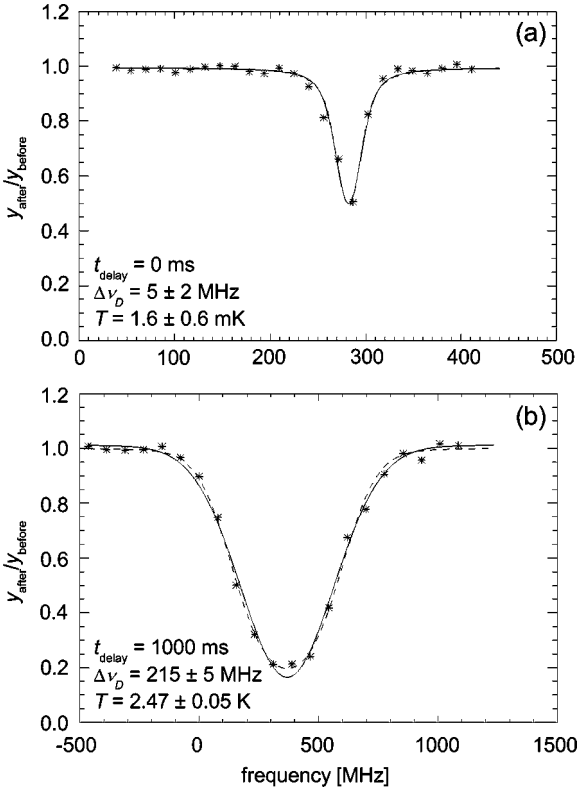

FIG. 4. Line profiles recorded for a spherical plasma of 440 000 ions at (a) $t_{\text{delay}}=0$ ms and (b) $t_{\text{delay}}=1000$ ms. The dashed and solid lines are Voigt profile fits respectively with [Eq. (5)] and without [Eq. (7)] saturation correction. In (a) the two fits are nearly identical. The Doppler widths and corresponding temperatures extracted from the fits with saturation correction are shown. The frequency scale is referenced to the center of the laser sweep interval, which generally does not coincide with the line center. For technical reasons, the frequency scales of (a) and (b) are shifted relative to each other. This shift is due to a change in the offset of the frequency sweep of the laser and is not an actual shift of the line center.

Figure 5(b) shows a close-up of the short-time heating rate data from Fig. 5(a). From linear fits to the data, heating rates around 65 mK/s are obtained. This is comparable to the heating rates observed in miniature radio-frequency traps typically used for pursuing ion-entanglement experiments. However, in the following section we argue that the source of heating in the miniature radio-frequency traps [20] is different from the source of heating in the present Penning trap.

B. Heating mechanisms

In this section, we investigate the importance of the different possible sources of energy: residual-gas collisions, work done by the rotating wall, and electric-field noise from the trap electrodes.

1. Residual-gas collisions

The effect of residual-gas collisions was investigated by recording heating rate curves at different residual-gas pressures (see Fig. 6). Data were taken at three different values

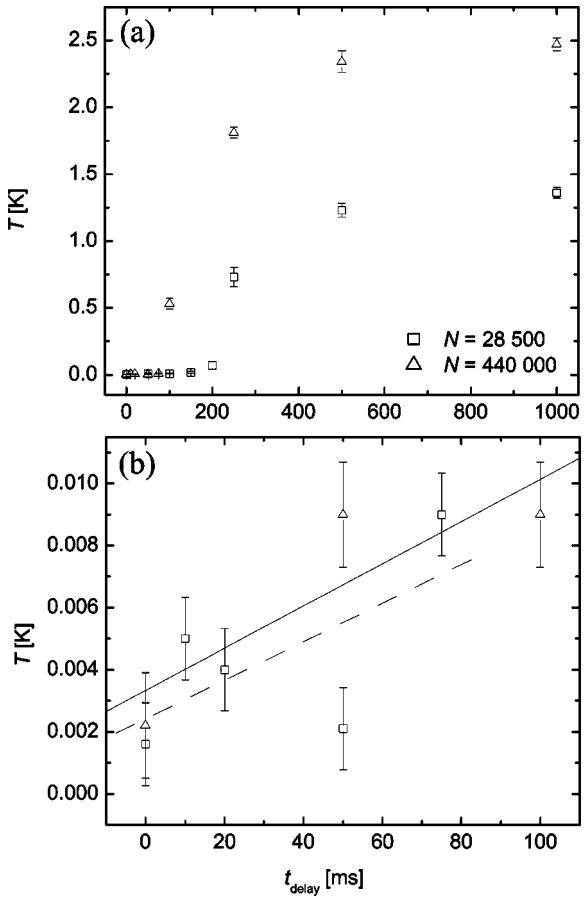

FIG. 5. (a) Heating-rate curves (temperature as a function of t_{delay}) for plasmas consisting of 28 500 and 440 000 ions. (b) A close-up of the short-time data where the plasmas are still in the solid phase. Linear fits to the short-time data give short-time heating rates of 68 ± 24 mK/s (solid) and 62 ± 21 mK/s (dashed), respectively, for the small and large plasma.

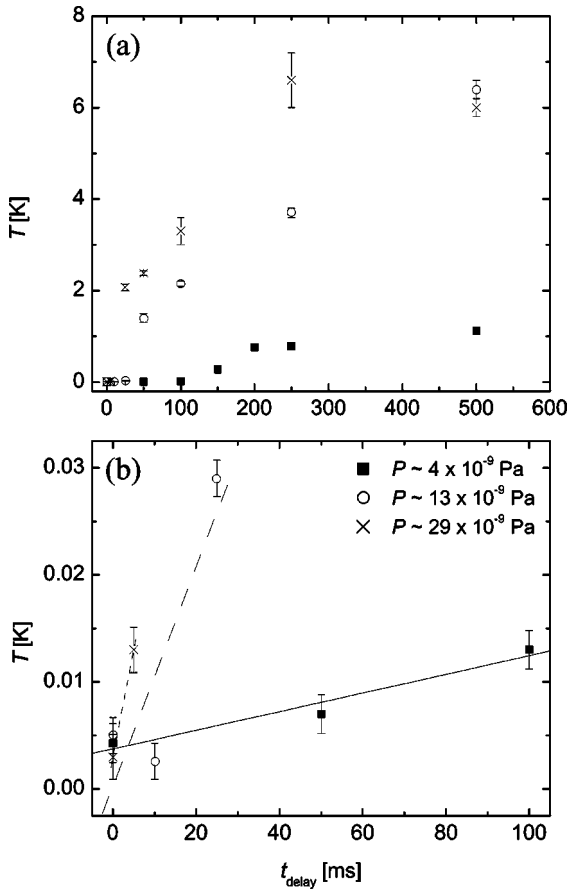

FIG. 6. (a) Heating-rate curves for a 410 000 ion plasma recorded at three different pressures. (b) A close-up on the short-time data where the plasma is still in the solid phase. Straight lines have been fitted to the short-time data yielding heating rates of 87 ± 19 mK/s (solid line), ~1.0 K/s (long-dashed line), and ~2.0 K/s (short-dashed line) for lowest, intermediate, and highest pressure, respectively.

of the pressure. When operating at the lowest pressure (at which the data in Fig. 5 were also recorded) the Bayard-Alpert ionization gauge, which measures the residual-gas pressure, is turned off and the exact value of the pressure is not known. We estimate that the base pressure, when the ionization gauge is off, is $\sim4\times10^{-9}$ Pa (see the Appendix). With the ionization gauge on, a pressure of $\sim13\times10^{-9}$ Pa was measured. A further increase in the pressure to $\sim29\times10^{-9}$ Pa was obtained by regularly cycling the ion pumps off and on.

An increased heating rate at elevated pressures is evident from linear fits to the short-time data shown in Fig. 6(b). The fits yield heating rates of 87 ± 19 mK/s, ~1.0, and ~2.0 K/s for the lowest, intermediate and highest pressures, respectively. Due to the limited number of data points in the solid phase, the heating rates for the intermediate and highest pressures are very uncertain. However, clear evidence of a correlation between residual gas pressure and heating is also found from the onset of rapid heating, which happens at delay times of around 100, 25, and 5 ms for the lowest, intermediate, and highest pressures, respectively [see Fig. 6(a)]. This heating starts at the solid-liquid phase transition which occurs at a fixed temperature $T\simeq10$ mK. Therefore, the observed shift of rapid heating to shorter times with elevated pressures shows that residual-gas collisions are a dominant heating mechanism while the plasma is in the solid phase. Finally, in the Appendix we estimate the ion heating rate due to residual-gas collisions for different ion-molecule collisional cross sections assuming that H_2 is the dominant background gas molecule. We obtain heating rate estimates that are 2–18 times larger than the measured 65 mK/s heating rate. Accordingly, residual-gas collisions are expected to be an important mechanism and can provide an explanation for the observed heating.

Residual-gas collisions are of less importance in the miniature radio-frequency traps holding just a few ions. For room-temperature traps at $\sim10^{-8}$ Pa, the collision rate per ion with the residual gas molecules is ~0.03 s^{-1} [28]. Hence, in the case where only a few ions are present in a trap under ultrahigh vacuum, the interval between two residual-gas collisions is sufficiently long that most measurements are carried out without any collision events. With 10^4–10^6 ions, on the other hand, residual-gas collisions are so frequent that it becomes necessary to take into account the average effect of those collisions.

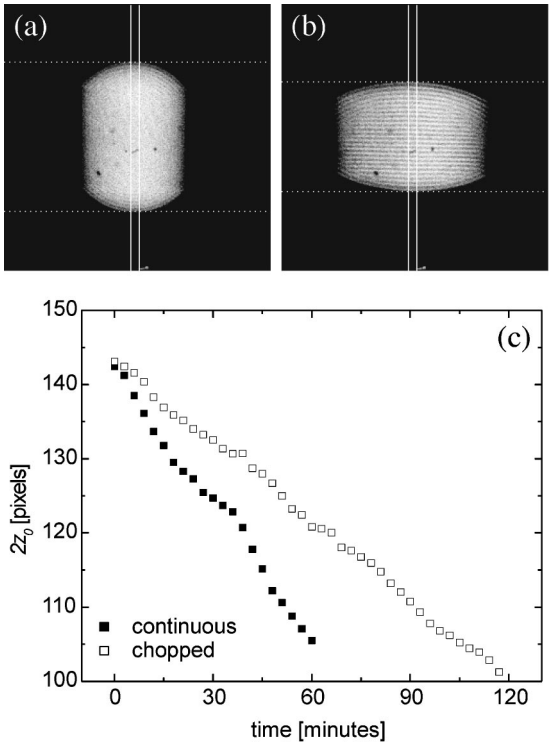

FIG. 7. Spin-down data for a plasma consisting of 25 000 ions. Two image sequences covering roughly the same range in rotation frequency were recorded, one with the axial cooling beam on continuously and one with the axial cooling beam chopped. The images are 256×256 pixels with 4 μm/pixel. (a) and (b) show the actual images corresponding to the highest and lowest rotation frequencies, respectively, in the run with a continuous cooling beam. (c) Plasma height as a function of time after turning off the rotating wall for continuous and chopped cooling beams.

2. Work done by the rotating wall

The torque due to the rotating wall was deduced from measurements of the plasma spin-down rate when the rotating wall was turned off. Equation (12) was then used to estimate the energy input due to the rotating wall. Figure 7 shows the results of a relatively long spin-down measurement. The spin-down rate is nearly twice as high in the data recorded with the cooling beam on continuously as in the data with the cooling beam chopped. This shows that the laser torque is the dominant torque. Also, the continuous and chopped runs are subject to inconsistent fluctuations in the spin-down rate, which we attribute to laser-torque fluctuations. In the derivation of Eq. (11), it is assumed that τ_{laser} is constant in time. In an attempt to minimize errors in the analysis caused by laser-torque fluctuations, we resort to taking image sequences of less than 15 min duration. Two subsequent image sequences, recorded with the cooling beam continuous and chopped, give measurements of τ_{cont} and τ_{chop}, respectively. An example obtained with a plasma consisting of 18 600 ions is shown in Fig. 8.

To gain better statistics and average over laser torque fluctuations, many image sequences are recorded, alternating between the cooling beam on continuously and chopped. Every two subsequent image sequences are then combined using

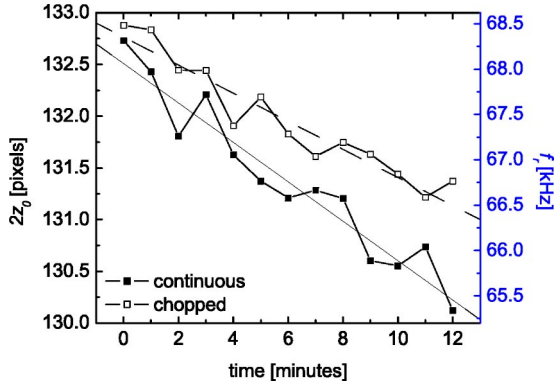

FIG. 8. The result of short-duration spin-down image sequences for a plasma consisting of 18 600 ions recorded with the cooling beam on continuously and chopped. Height and corresponding rotation frequency $f_r=\omega_r/2\pi$ are plotted as a function of time after turning off the rotating wall. Straight lines are fitted to the two data sets giving the spin-down rates. From these rates the torques $\tau_{\text{ext}}=3.5\times10^{-31}$ J and $\tau_{\text{laser}}=4.7\times10^{-31}$ J at $f_r=67$ kHz are extracted. This data set corresponds to run No. 11 in Fig. 9

Eq. (11) to determine τ_{ext} and τ_{laser}. The outcome of a complete data series taken on a 18 600 ion near-spherical plasma ($f_r=67$ kHz) is shown in Fig. 9. In Fig. 9(b) the work per ion per unit time due to the rotating wall is estimated from τ_{ext} and Eq. (12). This work is divided by the specific heat of an ideal gas to obtain an estimate of the possible temperature change due to this energy input. Averaging the results of Fig. 9(b) yields an estimate for the possible temperature change due to the work done by the rotating wall of

$$\left.\frac{1}{\frac{3}{2}k_B}\frac{dE}{dt}\right|_{\text{wall}} = -3\pm10\ \text{mK/s}. \tag{13}$$

Since the runs in Fig. 9 are not completely independent, and also because the laser torque fluctuations between runs are probably not random, we use the standard deviation of the group of measurements in Fig. 9(b) (without dividing by $\sqrt{N_{\text{run}}}$, where N_{run} is the number of runs) to obtain the uncertainty stated in Eq. (13). Interestingly, the anticorrelation between τ_{ext} and τ_{laser} evident in Fig. 9 is the expected behavior if the measurements are dominated by laser torque fluctuations. We can therefore only place an upper limit of 10 mK/s on the temperature increase due to the rotating wall. The specific heat of a crystallized strongly coupled plasma approaches $3k_B$, the specific heat of a harmonic lattice, for large couplings Γ. Use of this specific heat would result in a limit smaller by a factor of 2 on the temperature increase due to the rotating wall. In either case, this energy input is significantly below the heating rate obtained from the temperature measurements. Hence, the contribution to the heating rate from the rotating wall torque is negligible for a plasma of this size.

A similar data series obtained with a large plasma consisting of 440 000 ions is shown in Fig. 10. In this case, an energy input per ion from the rotating wall at $f_r=67$ kHz of

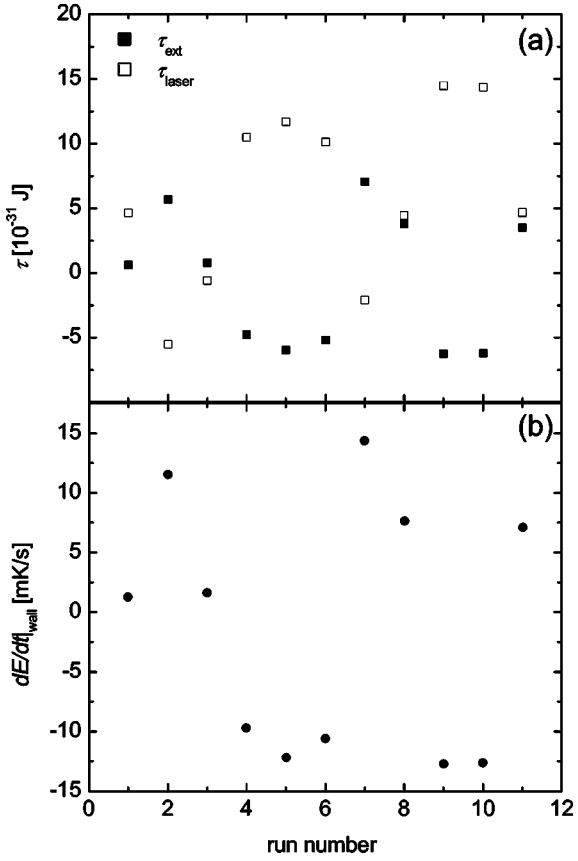

FIG. 9. Torques (a) and resulting work done by the rotating wall (b) at f_r=67 kHz (near-spherical) extracted from a complete series of spin-down measurements on a plasma consisting of 18 600 ions. Each run consists of a spin-down measurement with the cooling beam on continuously and chopped. The first run is based on the data from the first continuous and the first chopped measurements, and the second run is based on the data from the first chopped and the second continuous measurements, etc. The runs are therefore not completely independent.

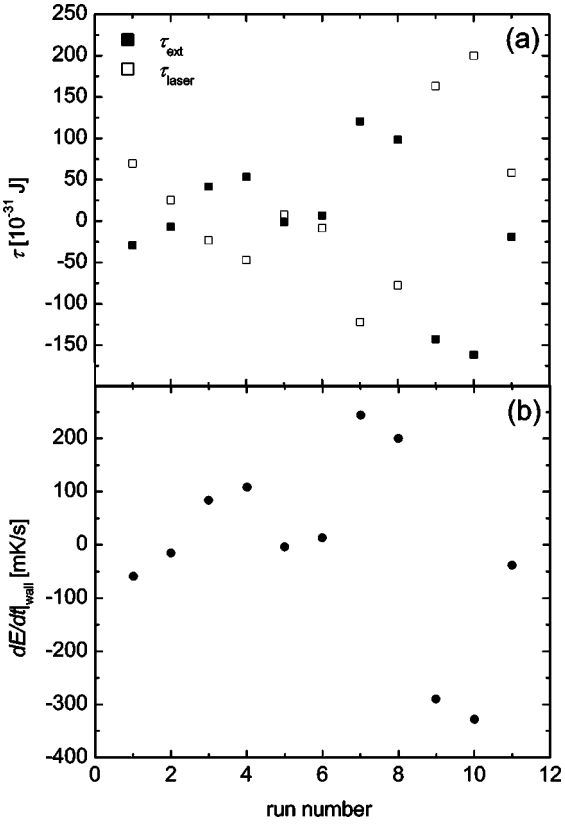

FIG. 10. Torques (a) and resulting work done by the rotating wall (b) at f_r=67 kHz (near-spherical) extracted from a complete series of spin-down measurements on a plasma consisting of 18 600 ions.

$$\left.\frac{1}{\frac{3}{2}k_B}\frac{dE}{dt}\right|_{\text{wall}} = -7 \pm 177 \text{ mK/s} \tag{14}$$

is obtained. Once again the uncertainty is dominated by laser torque fluctuations, and we can only place an upper limit of ~180 mK/s on a potential temperature increase due to the rotating wall. Even though we believe that the fluctuations in the axial laser beam direction and position are approximately the same in Figs. 9 (small plasma) and 10 (large plasma), the larger plasma appears to be approximately 20 times more sensitive to these fluctuations. Presumably this is because the magnitude of the laser torque fluctuations depend sensitively on the ratio of the plasma radius to the axial laser beam waist. For large plasmas the limit on the temperature increase due to the rotating wall is not small compared to the heating rate found by the temperature measurements. However, Fig. 6 shows that the heating rate of a large plasma sensitively depends on the background pressure. In addition, the measured short-time (solid phase) heating rate of a large plasma approximately equals that of a small plasma, which is shown to be due mainly to residual gas collisions. Therefore, residual gas collisions can account for the large plasma heating rate, although in this case we cannot rule out some contribution due to the rotating wall.

In addition to heating the ions, residual-gas collisions produce a drag on the rotating ion plasma, which will contribute to the plasma spin down. In the Appendix, we show that under some ideal assumptions it is possible to relate the heating due to residual-gas collisions to the torque due to the residual-gas drag. In particular, if the Be^+-residual-gas collisions are elastic, the average torque per ion due to residual-gas drag, τ_{drag}, is related to the average energy increase per ion due to residual-gas collisions, $(dE/dt)|_{\text{coll}}$, by

$$\tau_{\text{drag}} = \frac{2}{15}\frac{m+m_{\text{rg}}}{m_{\text{rg}}}\frac{\omega_r r_0^2}{v_{\text{rms}}^2}\left.\frac{dE}{dt}\right|_{\text{coll}}. \tag{15}$$

Here $v_{\text{rms}}=\sqrt{k_B T/m_{\text{rg}}}$ is the root-mean-square velocity of the residual gas and m_{rg} is the mass of the dominant residual-gas species. Equation (15) assumes a single-species plasma. If the residual gas consists of more than one dominant species, then Eq. (15) must be summed over the different species. Our dominant residual gas is presumably H_2. If the H_2 mass, a residual gas temperature of T=300 K, and a heating rate of 65 mK/s [Fig. 5(b)] are substituted into Eq. (15), we obtain values of 2.5×10^{-32} J and 2.0×10^{-31} J for the average

torque per ion due to residual-gas collisions for the small and large plasmas of Figs. 9 and 10. These torques are about two orders of magnitude less than the experimental limits obtained from Figs. 9 and 10 on the total torque per ion due to all sources, including residual-gas drag and ambient static field errors.

3. Electric-field noise

Heating in miniature radio-frequency traps due to electric field noise caused by both thermal electronic noise (Johnson noise) and fluctuating patch fields was studied in Ref. [20]. We make the simple assumption that these noise sources could be present at a comparable level in our Penning trap. The heating rates attributed to these two forms of noise are proportional to $1/d^2$ and $1/d^4$, respectively, where d is the characteristic distance from the trap electrodes to the ions [20]. In our Penning trap, the distance from the trap electrodes to the ions is larger by two orders of magnitude than in the miniature radio-frequency traps. The heating rates due to thermal electronic noise and fluctuating patch fields should therefore be decreased by four and eight orders of magnitude, respectively, compared to those for the miniature radio-frequency traps. Since the heating rates observed in these two different types of traps are of the same order of magnitude, we conclude that the contribution from electric-field noise to heating in our Penning trap should be negligible.

IV. CONCLUSION

The present study shows that the laser-cooled $^9Be^+$ plasmas in our Penning trap have a heating rate of 65 mK/s while in solid phase. For relatively small plasmas consisting of 20 000–30 000 ions, we have been able to establish that the heating is caused by residual-gas collisions. Residual-gas collisions also appear to be the main heating mechanism for large plasmas with ~400 000 ions. We note that the heating rate has been measured only for spherical plasmas, and that the relative importance of energy increase due to residual-gas collisions and the rotating wall could vary with the plasma rotation frequency and shape.

The solid-phase heating rate, valid for the first 100–200 ms, is comparable to the heating rates obtained in miniature radio-frequency ion traps, where entanglement of up to four ions has been achieved. Since large numbers of ions can be trapped and cooled in the present Penning trap, entanglement of many more ions may be possible. In general, the internal state manipulations used to entangle the ions slow down with increasing number of trapped ions. However, with the solid-phase heating rate measured here, we believe entanglement of between 100 and 1000 ions into spin-squeezed states with significant levels of squeezing should be within reach.

Finally, we note that the slow heating rate of the ions measured in the solid phase is followed by a very rapid heating in the liquid phase. This sudden change in the heating rate appears to be a manifestation of the solid-liquid phase transition. At present, we do not understand how the solid-liquid phase transition could produce this signature. This is, however, an interesting question to pursue in future experiments.

ACKNOWLEDGMENTS

This work was supported by the Office of Naval Research. One of the authors (T.H.) acknowledges the Nishina Memorial Foundation (Japan) for financial assistance. The authors thank Daniel H. E. Dubin for stimulating discussions and Wayne M. Itano and Tobias Schätz for useful comments on the paper.

APPENDIX

In this paper we have considered changes in the plasma energy due to residual-gas collisions, work done by the rotating wall, and heating due to electric field noise. If we neglect heating due to electric field noise, which we believe to be negligible, the energy increase per ion after the cooling laser beams are turned off can be written as

$$\frac{dE}{dt} = \left.\frac{dE}{dt}\right|_{\text{coll}} + \left.\frac{dE}{dt}\right|_{\text{wall}}. \tag{A1}$$

Here E, as in Eq. (12), is the total plasma energy (the sum of the potential and kinetic energies) per ion as calculated in the lab frame. The corresponding increase in the ion temperature can be obtained by dividing dE/dt by the specific heat. If the external torque opposing the plasma rotation is due to ambient static-field errors and residual gas drag, we may further write $\tau_{\text{ext}} = \tau_{\text{field}} + \tau_{\text{drag}}$ and, from Eq. (12):

$$\left.\frac{dE}{dt}\right|_{\text{wall}} = \omega_r \tau_{\text{field}} + \omega_r \tau_{\text{drag}}. \tag{A2}$$

In this appendix, we derive an expression for $(dE/dt)|_{\text{coll}}$ in terms of the residual gas density, temperature, and collision cross section. We derive a similar expression for the torque τ_{drag} due to the residual gas drag and relate this torque to $(dE/dt)|_{\text{coll}}$. We show that $\omega_r \tau_{\text{drag}}$, the work per unit time done by the rotating wall to balance the background gas drag, is small compared to $(dE/dt)|_{\text{coll}}$ and can be neglected.

We assume that the ions are cold ($T=0$), that the collisions are elastic, and that the rotational velocity of an ion is small compared to the thermal residual-gas velocity. That is, if $\mathbf{u} \equiv r\omega_r \hat{\theta}$ is the rotational velocity of an ion in the plasma and $v_{\text{rms}} \equiv \sqrt{kT_{\text{rg}}/m_{\text{rg}}}$ is the one-dimensional root-mean-square velocity of the residual-gas particles with mass m_{rg} and temperature T_{rg}, we assume $u \equiv |\mathbf{u}| \ll v_{\text{rms}}$ and calculate the energy change and drag due to residual-gas collisions to lowest nonvanishing order in u/v_{rms}.

1. Energy transfer due to collisions

For simplicity, we calculate the energy transfer due to a residual-gas collision with an ion in a local inertial frame moving with the ion's rotational velocity $\mathbf{u}$. We note that describing a residual-gas collision in such a local inertial reference frame makes sense because the duration of a

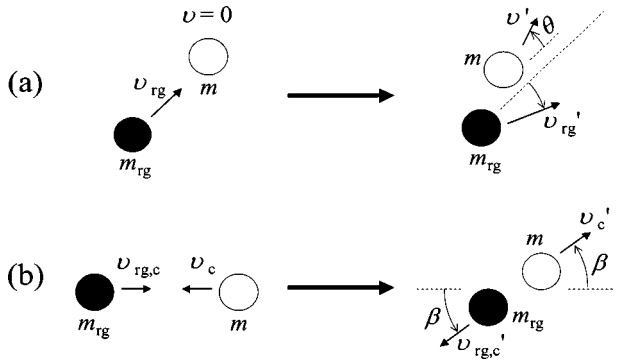

FIG. 11. Sketch of the initial and final states of a residual-gas collision in (a) the initial rest frame of the ion and (b) the center-of-mass frame. This figure defines quantities used in the text. The scattering angle θ of the ion in the rest frame is related to the scattering angle β in the center-of-mass frame by $\theta=\beta/2$.

residual-gas collision ($\lesssim$10 ps) is negligible compared to the rotation period ($2\pi/\omega_r \sim 20$ μs) of an ion. We show that the difference between the energy transfer calculated in this frame and the lab frame is small, of order $u^2/v_{\rm rms}^2$. It is frequently useful to describe the ion motion in a frame that rotates with the ion plasma [8]. In this rotating frame the ion energy E_R is given in terms of the lab frame energy E and canonical angular momentum L (about the z axis) by $E_R = E+\omega_r L$. In a residual-gas collision, the energy transferred to an ion in a local inertial frame moving with the ion's rotational velocity $\mathbf{u}$ is the same as the energy transfer calculated in the rotating frame.

For $T=0$, a trapped ion (i.e., a trapped Be^+ ion) is at rest in a local frame moving with the ion's rotational velocity $\mathbf{u}$. As shown in Fig. 11(a), let $v_{\rm rg}$ be the velocity of a residual particle before the collision. In the center-of-mass (c.m.) frame, the final collision state can be described by two scattering angles: β, defined in Fig. 11(b) as the angle between the final velocities and the initial collision axis, and an angle ζ that describes the azimuthal orientation of the final scattering plane about the initial collision axis. In the c.m. frame, it is easy to show that the final ion velocity is $v_c' = m_{\rm rg}v_{\rm rg}/(m_{\rm rg}+m)$. In the local frame of the ion [Fig. 11(a)], this gives a final ion velocity of

$$v' = 2\frac{m_{\rm rg}}{m_{\rm rg}+m}v_{\rm rg}\cos\left(\frac{\beta}{2}\right) \tag{A3}$$

and a final ion energy (a recoil energy) of

$$\frac{1}{2}m(v')^2 = \frac{mm_{\rm rg}^2}{(m_{\rm rg}+m)^2}v_{\rm rg}^2 2\cos^2\left(\frac{\beta}{2}\right). \tag{A4}$$

Let $\sigma_E(v_{\rm rg})$ denote the total collision cross section for energy transfer, defined by

$$\sigma_E(v_{\rm rg}) = 2\pi\int_0^\pi \sin(\beta)d\beta\frac{d\sigma}{d\Omega}2\cos^2\left(\frac{\beta}{2}\right). \tag{A5}$$

Here $d\sigma/d\Omega$ is the differential scattering cross section which we assume to be independent of ζ. Also, let

$$F(\mathbf{v}) = \frac{1}{(2\pi)^{3/2}v_{\rm rms}^3}\exp\left(-\frac{\mathbf{v}^2}{2v_{\rm rms}^2}\right) \tag{A6}$$

denote a Maxwell-Boltzmann distribution of velocities with $v_{\rm rms}=\sqrt{kT_{\rm rg}/m_{\rm rg}}$ as defined earlier. In the local frame of an ion, the distribution of residual-gas velocities is $F(\mathbf{v}_{\rm rg}+\mathbf{u})$. The average energy increase per unit time of an ion due to residual-gas collisions can then be written as

$$\left.\frac{dE_R}{dt}\right|_{\rm coll} = n_{\rm rg}\frac{mm_{\rm rg}^2}{(m_{\rm rg}+m)^2}\int d^3\mathbf{v}_{\rm rg}F(\mathbf{v}_{\rm rg}+\mathbf{u})v_{\rm rg}^3\sigma_E(v_{\rm rg}), \tag{A7}$$

where $n_{\rm rg}$ is the density of the residual-gas molecules. Here we use E_R to denote that Eq. (A7) gives the energy increase per ion, due to collisions, in the rotating frame of the plasma. Equation (A7) is just the recoil heating of an ion due to residual-gas collisions. With $|\mathbf{u}| \ll v_{\rm rms}$ we expand

$$F(\mathbf{v}_{\rm rg}+\mathbf{u}) \simeq F(\mathbf{v}_{\rm rg})\left[1-\frac{\mathbf{v}_{\rm rg}\cdot\mathbf{u}}{v_{\rm rms}^2}+O\left(\frac{u^2}{v_{\rm rms}^2}\right)\right]. \tag{A8}$$

We neglect the small $u^2/v_{\rm rms}^2$ term. The term linear in $\mathbf{v}_{\rm rg}$ will average to zero leading to the result

$$\left.\frac{dE_R}{dt}\right|_{\rm coll} \simeq n_{\rm rg}\frac{mm_{\rm rg}^2}{(m_{\rm rg}+m)^2}\langle v_{\rm rg}^3\sigma_E(v_{\rm rg})\rangle. \tag{A9}$$

Here, we use the notation $\langle g(\mathbf{v})\rangle$ to denote the average of a quantity $g(\mathbf{v})$ over the Maxwell-Boltzmann distribution $F(\mathbf{v})$, i.e., $\langle g(\mathbf{v})\rangle = \int d^3\mathbf{v}F(\mathbf{v})g(\mathbf{v})$. Within the approximations used to derive Eq. (A9), $(dE_R/dt)|_{\rm coll}$ is independent of $\mathbf{u}$ and is therefore the same for all ions.

We use two different cross sections to estimate the heating rate. In an ion-molecule collision, the electric field of the ion polarizes the colliding residual gas molecule, resulting in an attractive interaction $U(R)=-\alpha q^2/(8\pi\epsilon_0 R^4)$ at large ion-molecule separation R [28]. Here α is the polarizability of the molecule. For impact parameters less than a critical value $b_{\rm crit}=(\alpha q^2/\pi\epsilon_0\mu v_{\rm rg}^2)^{1/4}$, where μ is the reduced mass, the residual-gas molecule penetrates an angular momentum barrier and undergoes a close spiraling collision with the ion [29]. The Langevin cross section $\sigma_{\rm Langevin}(v_{\rm rg})=\pi b_{\rm crit}^2$ therefore provides a measure of the cross section for close collisions. Because energy and momentum can also be transferred by long-range collisions, we expect $\sigma_{\rm Langevin}$ may underestimate the ion heating rate. A more conservative estimate of the heating rate is obtained from the total collision cross section in a C_4/R^4 potential. With $C_4=\alpha q^2/(8\pi\epsilon_0)$, the total "elastic" cross section is $\sigma_{\rm elastic}(v_{\rm rg}) = \pi\Gamma(1/3)[\alpha q^2/(16\epsilon_0\hbar v_{\rm rg})]^{2/3}$ [28].

The pressure in the vacuum vessel was measured by a nude ionization gauge located $\sim$1 m from the trapped ions. The pressure reading was $\sim 7\times10^{-9}$ Pa ($\sim 5\times10^{-11}$ Torr). However, Fig. 6(a) indicates that this reading is limited by outgassing of the gauge and that the pressure with the gauge off is likely 2–4 times lower. Our vacuum vessel is constructed mainly of stainless steel and fused silica. In systems like this, H_2 is typically the dominant background gas, which is what we assume here. With the reduction by a factor of 2

in sensitivity of the ionization gauge for H_2, we estimate a background of $\sim 4\times 10^{-9}$ Pa of H_2 with the ionization gauge off. At 300 K, this corresponds to a density of residual H_2 molecules of $n_{\rm rg}\simeq 1.0\times 10^{12}$ m^{-3}.

In estimating the heating rate with Eq. (A9) we assume isotropic scattering $[d\sigma/d\Omega=\sigma/(4\pi)]$. For isotropic scattering the collision cross section for energy transfer is equal to the normal collision cross section $[\sigma_E(v_{\rm rg})=\sigma(v_{\rm rg})]$. With $\alpha(H_2)=0.82\times 10^{-30}$ m^3, $m_{\rm rg}=2m_p$, and $m=9m_p$ (m_p =proton mass), after evaluation of the integral in Eq. (A9), we obtain

$$\left.\frac{1}{\frac{3}{2}k_B}\frac{dE_R}{dt}\right|_{\rm Langevin} \simeq 0.15 \text{ K/s}, \tag{A10}$$

$$\left.\frac{1}{\frac{3}{2}k_B}\frac{dE_R}{dt}\right|_{\rm elastic} \simeq 1.2 \text{ K/s}. \tag{A11}$$

These estimated heating rates are approximately 2 and 18 times larger than the measured heating rate of 65 mK/s discussed in Sec. III A. If we use the specific heat of a harmonic lattice ($3k_B$) instead of the specific heat of an ideal gas, the estimated heating rate is lowered by a factor of two. The heating rates of the heavy-mass impurity ions (see Sec. II) are reduced by the mass factor in Eq. (A9). However, even for the extreme case of a plasma consisting of 50% $^9Be^+$ ions and 50% $m=34$ a.m.u. ions, the heating rates of Eqs. (A10) and (A11) are only reduced by $\sim$30%. The difference between the estimated and measured heating rate may indicate that the estimated residual-gas pressure is too high or that our assumption of isotropic elastic collisions is too simplistic. Nevertheless, these estimations shows that residual-gas collisions can provide an explanation for the measured solid-phase heating rate of 65 mK/s.

2. Momentum transfer due to collisions

We now derive an expression similar to Eq. (A9) for the average momentum transfer due to residual-gas collisions. The momentum transferred to the ion in the collision depicted in Fig. 11 will consist of a component along $\mathbf{v}_{\rm rg}$ (i.e., along the original collision axis) given by

$$\frac{mm_{\rm rg}}{m_{\rm rg}+m}\mathbf{v}_{\rm rg}2\cos^2\left(\frac{\beta}{2}\right), \tag{A12}$$

and a component perpendicular to $\mathbf{v}_{\rm rg}$. The perpendicular component will average to zero in the integration over the azimuthal scattering angle ζ. The average momentum per unit time transferred to an ion due to residual-gas collisions can then be written as

$$\left.\frac{d\mathbf{P}}{dt}\right|_{\rm coll} = n_{\rm rg}\frac{mm_{\rm rg}}{m_{\rm rg}+m}\int d^3\mathbf{v}_{\rm rg}F(\mathbf{v}_{\rm rg}+\mathbf{u})v_{\rm rg}\mathbf{v}_{\rm rg}\sigma_E(v_{\rm rg}). \tag{A13}$$

In the expansion of $F(\mathbf{v}_{\rm rg}+\mathbf{u})$ in Eq. (A8), only the term linear in $\mathbf{v}_{\rm rg}$ will not average to zero. We obtain

$$\begin{aligned}\left.\frac{d\mathbf{P}}{dt}\right|_{\rm coll} &\simeq -n_{\rm rg}\frac{mm_{\rm rg}}{m_{\rm rg}+m}\left\langle v_{\rm rg}\frac{\mathbf{v}_{\rm rg}\cdot\mathbf{u}}{v_{\rm rms}^2}\mathbf{v}_{\rm rg}\sigma_E(v_{\rm rg})\right\rangle \\ &= -\mathbf{u}n_{\rm rg}\frac{mm_{\rm rg}}{m_{\rm rg}+m}\left\langle v_{\rm rg}\frac{(\mathbf{v}_{\rm rg}\cdot\mathbf{u})^2}{v_{\rm rms}^2u^2}\sigma_E(v_{\rm rg})\right\rangle \\ &= -\mathbf{u}n_{\rm rg}\frac{mm_{\rm rg}}{m_{\rm rg}+m}\frac{1}{3}\left\langle v_{\rm rg}\frac{v_{\rm rg}^2}{v_{\rm rms}^2}\sigma_E(v_{\rm rg})\right\rangle \\ &\equiv -m\gamma\mathbf{u},\end{aligned} \tag{A14}$$

where the drag coefficient γ is given by

$$\gamma=\frac{n_{\rm rg}}{3v_{\rm rms}^2}\frac{m_{\rm rg}}{m_{\rm rg}+m}\langle v_{\rm rg}^3\sigma_E(v_{\rm rg})\rangle. \tag{A15}$$

In Eq. (A14) we have used the fact that the average containing $(\mathbf{v}_{\rm rg}\cdot\mathbf{u}/u)^2$ is the same for any components of $\mathbf{v}_{\rm rg}$. Evaluation of Eq. (A15) with the parameters used to obtain Eqs. (A10) and (A11) gives

$$\gamma_{\rm Langevin}=3.0\times 10^{-4}\ \text{s}^{-1}, \tag{A16}$$

$$\gamma_{\rm elastic}=2.5\times 10^{-3}\ \text{s}^{-1}. \tag{A17}$$

Because the measured heating rate was less than the estimated heating rates of Eqs. (A10) and (A11), the drag coefficient due to residual gas collisions is likely also less than the estimates of Eqs. (A16) and (A17).

Equations (A9) and (A14) for the energy and momentum change of an ion due to residual gas collisions both involve the same $\langle v_{\rm rg}^3\sigma_E(v_{\rm rg})\rangle$ average. It follows that:

$$\left.\frac{d\mathbf{P}}{dt}\right|_{\rm coll}=-\frac{\mathbf{u}}{3v_{\rm rms}^2}\frac{m_{\rm rg}+m}{m_{\rm rg}}\left.\frac{dE_R}{dt}\right|_{\rm coll}. \tag{A18}$$

From Eq. (A18) we calculate the torque per ion, averaged over a uniform density spheroidal plasma, due to residual-gas drag. For a plasma consisting of a single ion species of mass m, we obtain

$$\tau_{\rm drag}=\frac{2}{15}\frac{m+m_{\rm rg}}{m_{\rm rg}}\frac{\omega_r r_0^2}{v_{\rm rms}^2}\left.\frac{dE_R}{dt}\right|_{\rm coll}. \tag{A19}$$

With the substitution $(dE_R/dt)|_{\rm coll}\sim(dE/dt)|_{\rm coll}$ (see next section), this expression was used on two different plasmas in Sec. III B 2 to estimate the torque per ion due to residual gas drag. Also, from Eq. (A19) we see that $\omega_r\tau_{\rm drag}\propto(\omega_r^2r_0^2/v_{\rm rms}^2)(dE_R/dt)|_{\rm coll}$. Because $\omega_r r_0\ll v_{\rm rms}$, the work per unit time $\omega_r\tau_{\rm drag}$ done by the rotating wall to balance the residual-gas drag is small compared to the collisional recoil heating $(dE_R/dt)|_{\rm coll}$ of the plasma.

3. Laboratory versus rotating frame

We have calculated the energy and momentum transfer due to residual-gas collisions in a local inertial frame moving with an ion's rotational velocity $\mathbf{u}$. This is equivalent to calculating the energy and momentum transfer due to collisions in the rotating frame of the plasma. The momentum transfer due to a collision is independent of the frame of reference, and therefore our calculation of the residual-gas drag is

frame independent. The energy transfer due to collisions is not the same in the lab and rotating frames, but the difference is small. Consider an ion with rotational velocity $\mathbf{u}$ in the lab frame, which undergoes a residual gas collision that changes its velocity by $\delta\mathbf{v}$. The change in the ion energy in the lab frame $\Delta\epsilon=\frac{1}{2}m(\mathbf{u}+\delta\mathbf{v})^2-\frac{1}{2}u^2$ due to the collision is related to the change in the ion energy in the rotating frame $\Delta\epsilon_R=\frac{1}{2}m\delta v^2$ by $\Delta\epsilon=\Delta\epsilon_R+m\mathbf{u}\cdot\delta\mathbf{v}$. In terms of the change in the momentum of the ion, $\Delta\mathbf{p}=m\delta\mathbf{v}$, this expression can be written $\Delta\epsilon=\Delta\epsilon_R-\omega_r\hat{z}\cdot(\mathbf{r}\times\Delta\mathbf{p})$. After averaging over the residual gas velocity distribution and over the ions in the plasma we obtain

$$\left.\frac{dE}{dt}\right|_{\text{coll}} = \left.\frac{dE_R}{dt}\right|_{\text{coll}} - \omega_r \left.\frac{dL}{dt}\right|_{\text{coll}}. \tag{A20}$$

Here, as before, E is the total plasma energy per ion and L is the canonical angular momentum per ion about the z axis in the lab frame. Equation (A20) also follows directly from the equation $E_R=E+\omega_r L$. From $(dL/dt)|_{\text{coll}}=\tau_{\text{drag}}$ we see that the energy increase due to collisions is reduced in the lab frame from the rest frame by the term $\omega_r\tau_{\text{drag}}$. As discussed earlier, this term is proportional to $(\omega_r^2 r_0^2/v_{\text{rms}}^2)(dE/dt)|_{\text{coll}}$ and, with the assumption $u\ll v_{\text{rms}}$, can be neglected compared to $(dE/dt)|_{\text{coll}}$.

Physically the term $-\omega_r(dL/dt)|_{\text{coll}}=-\omega_r\tau_{\text{drag}}$ in Eq. (A20) can be thought of as the work done by the ions in "spinning up" the residual gas. Not only is this work by the ions small compared to $(dE/dt)|_{\text{coll}}$, but it is offset by the work of the rotating wall in holding the plasma rotation frequency constant against the residual-gas drag. Mathematically if Eqs. (A2) and (A20) are substituted into Eq. (A1) we obtain

$$\frac{dE}{dt} = \left.\frac{dE_R}{dt}\right|_{\text{coll}} + \omega_r\tau_{\text{field}}. \tag{A21}$$

That is, the energy increase of an ion, after the cooling lasers are turned off, is due to collisional recoil heating $(dE_R/dt)|_{\text{coll}}$ and the work done by the rotating wall to counteract the torque due to ambient field errors $\omega_r\tau_{\text{field}}$. We note that $\omega_r\tau_{\text{drag}}$ does not enter in Eq. (A21).

[1] L. Hornekær and M. Drewsen, Phys. Rev. A **66**, 013412 (2002).
[2] W. M. Itano, J. J. Bollinger, J. N. Tan, B. Jelenković, X.-P. Huang, and D. J. Wineland, Science **279**, 686 (1998).
[3] T. B. Mitchell, J. J. Bollinger, D. H. E. Dubin, X.-P. Huang, W. M. Itano, and R. H. Baughman, Science **282**, 1290 (1998).
[4] H. F. Powell, D. M. Segal, and R. C. Thompson, Phys. Rev. Lett. **89**, 093003 (2002).
[5] *Non-Neutral Plasma Physics IV*, edited by F. Anderegg, C. F. Driscoll, and L. Schweikhard, AIP Conf. Proc. No. 606 (AIP, Melville, NY, 2002).
[6] S. Ichimaru, Rev. Mod. Phys. **54**, 1017 (1982).
[7] S. Ichimaru, H. Iyetomi, and S. Tanaka, Phys. Rep. **149**, 91 (1987).
[8] D. H. E. Dubin and T. M. O'Neil, Rev. Mod. Phys. **71**, 87 (1999).
[9] J. H. Malmberg and T. M. O'Neil, Phys. Rev. Lett. **39**, 1333 (1977).
[10] D. H. E. Dubin, Phys. Rev. A **42**, 4972 (1990).
[11] M. Kitagawa and M. Ueda, Phys. Rev. A **47**, 5138 (1993).
[12] D. J. Wineland, J. J. Bollinger, W. M. Itano, and D. J. Heinzen, Phys. Rev. A **50**, 67 (1994).
[13] J. J. Bollinger, W. M. Itano, D. J. Wineland, and D. J. Heinzen, Phys. Rev. A **54**, R4649 (1996).
[14] J. I. Cirac and P. Zoller, Phys. Rev. Lett. **74**, 4091 (1995).
[15] A. Sørensen and K. Mølmer, Phys. Rev. A **62**, 022311 (2000).
[16] D. Leibfried, *et al.*, Nature (London) **422**, 412 (2003).
[17] D. J. Larson, J. C. Bergquist, J. J. Bollinger, W. M. Itano, and D. J. Wineland, Phys. Rev. Lett. **57**, 70 (1986).
[18] J. J. Bollinger, J. D. Prestage, W. M. Itano, and D. J. Wineland, Phys. Rev. Lett. **54**, 1000 (1985).
[19] X.-P. Huang, J. J. Bollinger, T. B. Mitchell, and W. M. Itano, Phys. Rev. Lett. **80**, 73 (1998).
[20] Q. A. Turchette, D. Kielpinski, B. E. King, D. Leibfried, D. M. Meekhof, C. J. Myatt, M. A. Rowe, C. A. Sackett, C. S. Wood, W. M. Itano, C. Monroe, and D. J. Wineland, Phys. Rev. A **61**, 063418 (2000).
[21] T. B. Mitchell, J. J. Bollinger, W. M. Itano, and D. H. E. Dubin, Phys. Rev. Lett. **87**, 183001 (2001).
[22] J. M. Kriesel, J. J. Bollinger, T. B. Mitchell, L. B. King, and D. H. E. Dubin, Phys. Rev. Lett. **88**, 125003 (2002).
[23] J. J. Bollinger, D. J. Heinzen, F. L. Moore, W. M. Itano, D. J. Wineland, and D. H. E. Dubin, Phys. Rev. A **48**, 525 (1993).
[24] A laser beam with a waist w has an electric field $E\propto e^{-r^2/w^2}$, where r is the distance from the the center of the laser beam.
[25] L. R. Brewer, J. D. Prestage, J. J. Bollinger, W. M. Itano, D. J. Larson, and D. J. Wineland, Phys. Rev. A **38**, 859 (1988).
[26] Z.-C. Yan, M. Tambasco, and G. W. F. Drake, Phys. Rev. A **57**, 1652 (1998).
[27] W. M. Itano and D. J. Wineland, Phys. Rev. A **25**, 35 (1982).
[28] D. J. Wineland, C. Monroe, W. M. Itano, D. Leibfried, B. King, and D. M. Meekhof, J. Res. Natl. Inst. Stand. Technol. **103**, 259 (1998).
[29] J. B. Hasted, *Physics of Atomic Collisions*, 2nd ed. (American Elsevier, New York, 1972).